

Annealing in variational inference mitigates mode collapse: A theoretical study on Gaussian mixtures

Luigi Fogliani^{1,2}, Bruno Loureiro¹, and Marylou Gabrié²

¹Departement d’Informatique, École Normale Supérieure, Université PSL, CNRS

²Laboratoire de Physique de l’École Normale Supérieure, Université PSL, CNRS

Abstract

Mode collapse — the failure to capture one or more modes when targetting a multimodal distribution — is a central challenge in modern variational inference. In this work, we provide a mathematical analysis of annealing-based strategies for mitigating mode collapse in a tractable setting: learning a Gaussian mixture, where mode collapse is known to arise. Leveraging a low-dimensional summary statistics description, we precisely characterize the interplay between the initial temperature and the annealing rate, and derive a sharp formula for the probability of mode collapse. Our analysis shows that an appropriately chosen annealing scheme can robustly prevent mode collapse. Finally, we present numerical evidence that these theoretical trade-offs qualitatively extend to neural network-based models, Real-NVP normalizing flows, providing guidance for designing annealing strategies mitigating mode collapse in practical variational inference pipelines.

1 Introduction

Variational inference is a widely used framework for approximating complex probability distributions in settings where direct sampling is computationally prohibitive, with applications ranging from scalable Bayesian inference in machine learning to the sampling of Boltzmann distributions and free-energy landscapes in physics, chemistry, and materials science. Given a target distribution π , variational inference (VI) replaces the task of sampling from π with that of finding, within a family of candidate distributions \mathcal{Q} , the probabilistic model q that best approximates π . The variational family \mathcal{Q} is restricted to distributions that are easy to sample from and whose probability density function, also denoted by q , is known, normalization included. These requirements make the reverse Kullback–Leibler (KL) divergence

$$\mathcal{D}_{\text{KL}}(q|\pi) = \mathbb{E}_q \left[\log \frac{q(x)}{\pi(x)} \right] \quad (1.1)$$

a tractable criterion for selecting q , and allow samples from q to be used a posteriori as proxies for samples from π . Notably, optimizing $\mathcal{D}_{\text{KL}}(q|\pi)$ with respect to q does not require having knowledge of the normalization of π . Rooted in statistical mechanics Weiss (1907), VI was later popularized in Bayesian statistics Jordan et al. (1999); Blei et al. (2017), in particular for its good scaling properties. Moreover, advances in deep generative modelling have greatly expanded the class of tractable variational distributions, with normalizing flows providing flexible parameterizations that retain both easy sampling and tractable probability densities Rezende and Mohamed (2015); Albergo et al. (2019) and autoregressive networks providing the equivalent for discrete variables Wu et al. (2019).

However, a class of target distributions poses a significant challenge to VI, namely multimodal distributions. The reverse KL objective is well known to be mode seeking Jordan et al. (1999); Minka (2005), yielding approximations that concentrate on a subset of the target modes, a phenomenon commonly referred to as mode collapse. Increasing the expressivity of variational families through deep generative models does not, in general, alleviate this issue Noé et al. (2019); Hackett et al. (2021); Nicoli et al. (2023); Blessing et al. (2024); Soletskyi et al. (2025); Grenioux et al. (2025). Intuitively, mode collapse arises from the strong

penalty imposed by the reverse KL on assigning probability mass to regions where π is small, in particular the low-probability regions separating modes.

Various empirical strategies have been proposed to mitigate mode collapse in VI in the context of different fields of applications including molecular simulations [Noé et al. \(2019\)](#), classical and quantum field theories [Wu et al. \(2019\)](#); [Vaitl et al. \(2022\)](#); [Nicoli et al. \(2023\)](#) and Bayesian inference [Wang et al. \(2025\)](#). Among them, a widely applicable approach when optimization of the reverse KL is performed iteratively, typically using stochastic gradient descent, is to combine VI with annealing. Rather than targeting π directly, the variational distribution q is first optimized to approximate a tempered distribution proportional to π^β with $\beta < 1$, for which modes are typically connected. The temperature is then progressively lowered during optimization until $\beta = 1$ is reached. The early phases of optimization at high “temperature” $1/\beta$ promote exploration and mitigate mode collapse. Annealed VI has been successfully applied to sampling from Boltzmann distributions in statistical mechanics [Wu et al. \(2019\)](#); [Schopmans and Friederich \(2025\)](#), to sampling from Bayesian posteriors [Huang et al. \(2018\)](#); [Wang et al. \(2025\)](#), and to optimization tasks, including locating multiple modes [LeMinh et al. \(2025\)](#) or identifying global minima [Hibat-Allah et al. \(2021\)](#); [Khandoker et al. \(2025\)](#).

Despite the major challenge posed by mode-collapse and the practical successes that annealing has brought, little theoretical work has focused on gaining understanding around its behavior. In this work, we make a first step in closing this gap by investigating annealing in a tractable multimodal VI setting where the target is a bimodal Gaussian mixture with well-specified variational family, in which the parameters of the variational model are trained by gradient flow. Our **main contributions** are:

- First, we show that mode collapse can be systematically avoided in this setting by employing a suitable annealing schedule, including in parameter regimes where collapse is otherwise unavoidable. These experiments reveal a critical trade-off between the initial temperature and the annealing rate, which must be carefully balanced to reliably recover all target modes.
- We identify a set of relevant summary statistics which enable to recast the high-dimensional gradient flow into a low-dimensional dynamical system, allowing to tractably identify distinct high- and low-temperature dynamical regimes and derive a closed-form expression for the mode collapse probability that quantitatively captures the aforementioned experimental trade-off.
- We show that the previous findings extend to a practical and expressive choice of variational family, RealNVP normalizing flows [Dinh et al. \(2017\)](#). This suggests that our theoretical results can provide guidance for the design of annealing schedules in practical pipelines.

Related works. Theoretical investigation of mode collapse in VI has received little attention to this day. By studying the gradient flow associated with variational inference over Gaussian mixtures with fixed weights, [Huix et al. \(2024\)](#) obtained theoretical guarantees in a setting related to the one considered below. Their analysis, however, was not concerned with multimodal target distributions and did not investigate the mode-collapse phenomenon. [Petit-Talamon et al. \(2025\)](#) investigated variational inference with Gaussian mixture variational families through gradient-flow-based algorithms, emphasizing computational and algorithmic aspects, while leaving the analysis of mode collapse unexamined. An exception is [Soletskyi et al. \(2025\)](#), from which the present paper draws inspiration.

Building on ideas from statistical physics of learning [Saad and Solla \(1995\)](#), [Soletskyi et al. \(2025\)](#) derived a summary statistics description for VI on a bimodal Gaussian mixture. A key difference with respect to our work is that in [Soletskyi et al. \(2025\)](#) the variance is kept fixed, making the description not amenable to the study of annealing. Further, [Soletskyi et al. \(2025\)](#) showed that the probability of occurrence of mode-collapse is controlled by the distance between modes of the target mixture with a critical radius R_c , function of the class imbalance, above which the dynamics from an uninformed initialization is highly likely to collapse on one mode. Using a similar setup, keeping the weights fixed for simplicity, the present works extends the analysis to learnable variances, a key ingredient to study annealing which changes the effective variance of the target model along the training dynamics.

Finally, annealing was previously identified as a mean to avoid collapse in VI powered by modern generative models by several authors as already cited in the introduction [Wu et al. \(2019\)](#); [Schopmans and Friederich \(2025\)](#); [Huang et al. \(2018\)](#); [Wang et al. \(2025\)](#); [LeMinh et al. \(2025\)](#); [Hibat-Allah et al. \(2021\)](#);

Khandoker et al. (2025). Used as an heuristic method, little guidance is provided in these works on how to adjust the annealing schedule. An exception is Wang et al. (2025), which proposes an adaptive schedule for the annealing speed based on the instantaneous effective sample size of proposals from a normalizing flow along its training by VI. Comparatively, the adjustment of annealing methods has been extensively discussed in the context of Monte Carlo samplers such as parallel tempering Syed et al. (2021) or sequential Monte Carlo Barzegar et al. (2024) and optimizers with simulated annealing Hajek (1988); Nadler and Hansmann (2007).

2 Setup and preliminary experiments

2.1 Annealed VI with bimodal Gaussian mixtures

We consider a minimal multimodal model for mode collapse in VI, where both π and q are mixtures of two isotropic Gaussian distributions on \mathbb{R}^d :

$$\begin{aligned}\pi(x) &= w_* \mathcal{N}(x|\mu_*, I_d) + (1 - w_*) \mathcal{N}(x|-\mu_*, I_d), \\ q_\theta(x) &= w_1 \mathcal{N}(x|\mu_1, \sigma_1^2 I_d) + (1 - w_1) \mathcal{N}(x|\mu_2, \sigma_2^2 I_d),\end{aligned}\tag{2.1}$$

where $w_*, w_1 \in [0, 1]$, $\mu_*, \mu_1, \mu_2 \in \mathbb{R}^d$ and $\sigma_1, \sigma_2 \in \mathbb{R}_+$. Here the trainable parameters of the variational distribution q_θ are the two means and the two standard deviations: $\theta = (\mu_1, \mu_2, \sigma_1, \sigma_2) \in \mathbb{R}^{2(d+1)}$. To simplify the discussion, we fix the weights and chose $w_1 = w_2 = 0.5$ in order not to break the symmetry between the modes of the variational model. Following Soletskyi et al. (2025) we constrain the means to lie on a sphere $\mu_*, \mu_{1,2} \in \mathbb{S}^{d-1}(R)$, which further simplifies the analytical treatment without affecting the qualitative behavior of the model. In this setup, q_θ is referred to as the student distribution.

As discussed in the introduction, given the variational family q_θ , annealed-VI consists of learning θ by minimizing the reverse Kullback-Leibler divergence loss between q_θ and the tempered distribution proportional to π^β where $1 > \beta > 0$ is the inverse temperature. Denoting by \mathcal{Z}_β the normalization constant of the tempered distribution, the effective loss is

$$\begin{aligned}\mathcal{L}(\theta, \beta) &= \mathcal{D}_{\text{KL}}\left(q_\theta \parallel \frac{\pi^\beta}{\mathcal{Z}_\beta}\right) \\ &= \mathbb{E}_{q_\theta}[\log q_\theta(x)] - \beta w_1 \mathbb{E}_{\mathcal{N}(\mu_1, \sigma_1^2 I_d)}[\log \pi(x)] \\ &\quad - \beta w_2 \mathbb{E}_{\mathcal{N}(\mu_2, \sigma_2^2 I_d)}[\log \pi(x)] - \log \mathcal{Z}_\beta.\end{aligned}\tag{2.2}$$

The first term in eq. (2.2) is the entropy of q_θ , which favors exploration pushing μ_1 and μ_2 apart. The two following terms are the cross-entropy between q_θ and π , each of them attracting μ_1 and μ_2 , separately, at $\pm \mu_*$. The last term is a constant with respect to θ and is omitted in the following. The parameter β tunes the relative importance between student entropy and cross-entropy with the target, higher temperatures (i.e. lower β) encouraging exploration.

In practice, $\mathcal{L}(\theta, \beta)$ is minimized with a descent-based algorithm. For simplicity, here we will focus on the spherical gradient flow with learning rate $\eta_\theta > 0$:

$$\dot{\theta}(t) = -\eta_\theta \nabla_\theta^{\mathbb{S}^{d-1}(R)} \mathcal{L}(\theta(t), \beta(t)),\tag{2.3}$$

from an initial $\mu_{1,2}$ uniformly sampled from $\mathbb{S}^{d-1}(R)$, with $\beta(t)$ progressively annealed throughout the trajectory from an initial high-temperature ($\beta < 1$) to the target temperature ($\beta = 1$). In particular, we employ the JKO scheme Jordan et al. (1998) on a geometry adapted for isotropic Gaussian mixtures proposed by Petit-Talamon et al. (2025), which allows to relate the learning rate of the means (η_μ) with the learning rate of the standard deviations (η_σ) in a principled way: $\eta_\sigma = \eta_\mu/d$ (see Appendix A).

As shown by Soletskyi et al. (2025), despite its simplicity this setting displays a sufficiently rich phenomenology to investigate mode collapse, and offers the perfect playground to understand how simulated annealing can mitigate it. As we will discuss in the following, our results considerably extend the scope of this work by considering trainable variances for the student. This ingredient is crucial for investigating annealing, as the annealing temperature directly acts on the effective variance of the tempered target π^β .

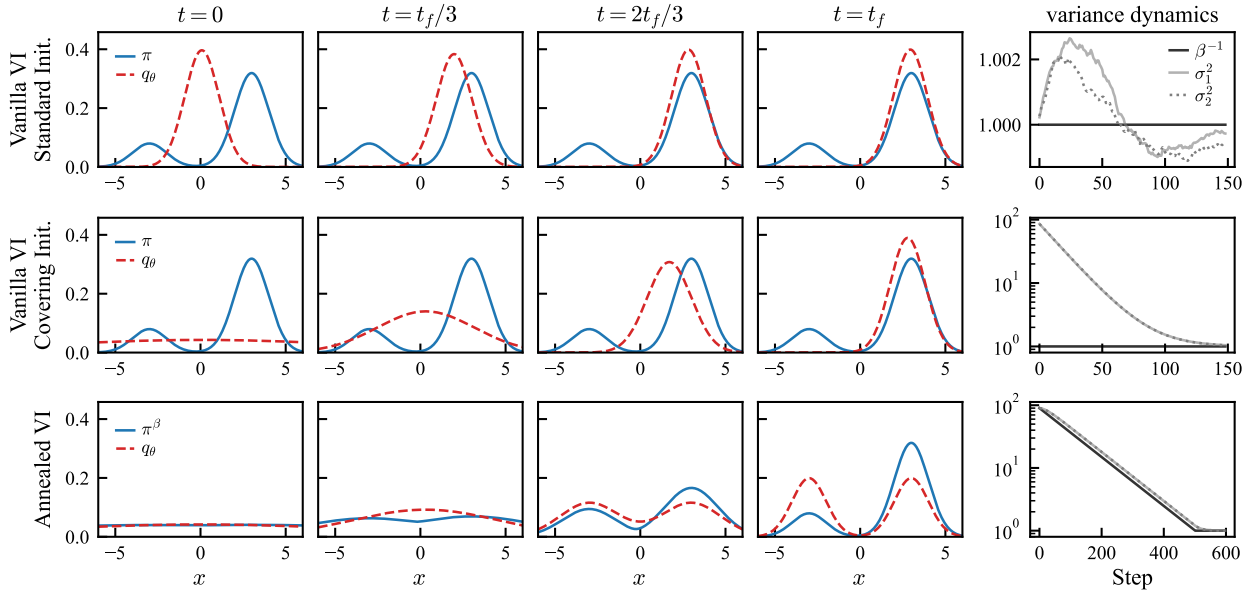


Figure 1: *Preliminary experiments: annealing mitigates mode collapse.* The first 4 columns show the marginal density along the direction of μ_* of both π and q_θ , at 4 different training stages. The fifth column shows the variance dynamics. Each row represents a different scenario; from top to bottom: no annealing with $\sigma_{1,2}$ initialized to one, no annealing with covering initial distribution (high initial variances $\sigma_{1,2} \gg R$), annealing with schedule given by eq. (2.4). Hyperparameters values are: $d = 512, R = 3, w_* = 0.8, w_1 = 0.5$ and learning rate $\eta = 0.05$.

More generally, it allows the student to have a wider distribution, which is believed to be important to avoid mode collapse in VI.

As a starting point, we consider a set of preliminary numerical experiments that will provide us guidance and illustrate interesting phenomenology for the discussion that follows.

2.2 Preliminary experiments

We consider a set up where the probability of mode collapse is high with vanilla VI ($\beta = 1$ fixed), setting the parameters of π to $R = 3$ (greater than the R_c , the onset radius for mode collapse as characterized in [Soletskyi et al. \(2025\)](#)), $w_* = 0.8$ and $w_1 = 0.5$ in dimension $d = 512$. [fig. 1](#) illustrates the learning dynamics of q_θ with three different learning strategies.

Vanilla VI with an initial variance equal to 1 leads to a collapse of μ_1 and μ_2 to the same mode of π (first row). Furthermore, the variances σ_1 and σ_2 remain close to 1 throughout the descent, suggesting that the learning dynamics are not very different from the fixed variance setup and, effectively, that trainable variances alone are not sufficient to avoid mode collapse.

A natural idea to avoid mode collapse is to improve the initialization of the gradient descent algorithm by increasing the initial variance of the modes of q_θ to make it overlap with the two modes of π . This can be done by setting the initial variances $\sigma_{1,2}^2 = O(R^2)$ (second row of [fig. 1](#)). Yet, the two modes still collapse to the same mode, and variances rapidly converge to 1. Moreover, when fixing the values of $\sigma_{1,2}$ to their initial large value, we still observe mode collapse on the same mode (see [Appendix fig. 6](#) first row) and interestingly the variances converge to the target value of 1 even if we freeze the means (see the second row of [fig. 6](#) in the Appendix).

Finally, we find instead that the learning dynamics with an annealing schedule of the form:

$$\beta(t) = \min(\beta_i^{1-t/t_0}, 1), \quad (2.4)$$

with $\beta_i^{-1} = 10R^2$ and $t_0 = 500$ (third row of fig. 1), avoids mode collapse. Variances are initialized to $1/\beta_i$ and interestingly, stay close to $1/\beta(t)$ throughout the learning dynamics.

These observations illustrate the typical phenomenology observed by practitioners performing VI on a multimodal target distribution with a flexible variational family. Despite a covering initialization, mode collapse can still occur and suitable annealing can be a mean to avoid it. However, choosing the right parameters — namely the initial temperature β_i and annealing time t_0 — is crucial to successfully avoid mode collapse. Next, we look closer at this dependency.

Influence of annealing schedule. While the efficacy of temperature annealing is well-documented in practice, the selection of an effective schedule remains a non-trivial challenge. To investigate this, we evaluate the impact of the annealing schedule in our controlled setting with an exponential form for $\beta(t)$ given in eq. (2.4). This choice is motivated by its parameter parsimony and the analytical findings that will follow, which suggest that preventing mode collapse requires the dynamics to remain in a high-temperature regime (specifically, $\beta < 1/R^2$) for a sufficient duration.¹

fig. 2 reports the probability of mode-collapse over a grid of annealing times (t_0) and initial inverse temperatures (β_i) for the same experimental set up as fig. 1. We observe a trade-off: if β_i is too high (low initial temperature), the system crosses the $1/R^2$ threshold too rapidly to resolve the target distribution's modes, leading to irreversible collapse. Conversely, while a very low β_i provides better exploration, it necessitates a significantly longer annealing time to avoid mode collapse leading to a higher computational budget. This implies the existence of an optimal β_i that balances modal resolution with convergence speed. Our analytical analysis, presented next, leads to an estimation of the mode collapse probability consistent with these empirical observations (0.5 isoprobability line predicted by theory represented by the black dashed line on fig. 2). Further below, we also show that these observations hold qualitatively for more complex variational families, namely RealNVPs.

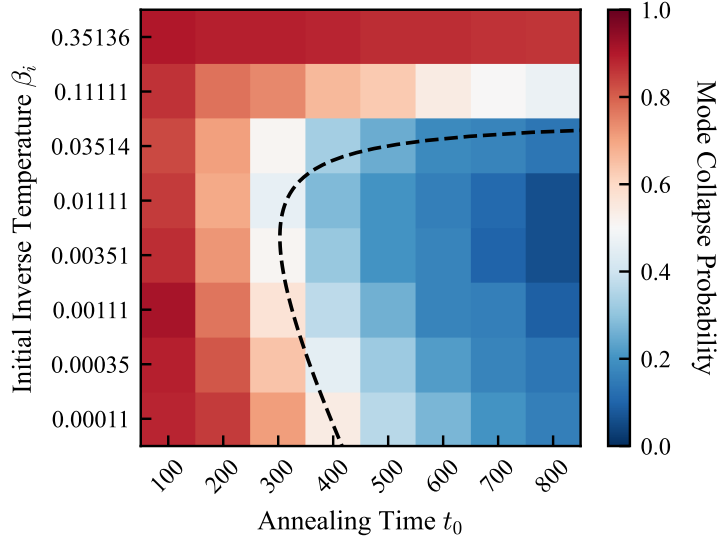


Figure 2: *Annealed VI mode collapse probability with Gaussian mixture student.* The form of the annealing scheme is fixed by eq. (2.4) and different values of the initial temperature β_i and annealing time t_0 are explored. Hyperparameters are the same as in fig. 1. For each values of (β_i, t_0) , the mode collapse probability is obtained using 100 different random student mean initialization. The dashed black line is the 0.5 mode collapse isoprobability line obtained with the analytical estimate of eq. (3.7).

¹For instance, annealing schemes of the form $\beta(t) = \beta_i + (1 - \beta_i)(1 - e^{-t/t_0})$ comparatively stay longer in the low temperature regime, which does not help avoiding mode collapse.

3 Analytical analysis

Our goal in this section is to give mathematical grounding to the numerical discussion of section 2.2. Our analysis builds on a low-dimensional reduction of the gradient flow dynamics in eq. (2.3), which we discuss in detail in section 3.1. Leveraging this description, we precisely characterize the probability of mode collapse for different choices of initial temperature and annealing rate, showing that a well-tempered annealing schedule is able to successfully mitigate mode collapse.

3.1 Summary statistics learning dynamics

Consider the gradient flow dynamics on $\mathcal{L}(\theta, \beta)$ introduced in eq. (2.3). Recall that our preliminary numerical experiments (fig. 1) showed that the student variances closely track the temperature during annealing: $\sigma_1^2(t) \approx \sigma_2^2(t) \approx \beta(t)^{-1}$. Based on this observation, we consider the following quasi-static approximation.

Assumption 3.1 (Variance approximation). Throughout the gradient flow trajectory, we assume that

$$\sigma_1^2(t) = \sigma_2^2(t) = \beta(t)^{-1}. \quad (3.1)$$

Further justification for this assumption is provided in section C.1. Assumption 3.1 simplifies the otherwise cumbersome dynamics of the variances, allowing us to focus on the trajectory of the means $\mu_{1,2}$, which explicitly reads

$$\dot{\mu}_c(t) = \left(I_d - \frac{\mu_c(t)\mu_c(t)^\top}{R^2} \right) \nabla_{\mu_c} \mathcal{L}(\theta(t), \beta(t)), \quad (3.2)$$

where $c \in \{1, 2\}$ and the student's means $\mu_c(0)$ are initialized uniformly on the sphere $\mathbb{S}^{d-1}(R)$.

The key idea of our analysis is to note that the reverse-KL loss $\mathcal{L}(\mu_{1,2}, \beta)$ can be equivalently described in terms of the following three scalar quantities, akin to *order parameters* in statistical physics

$$m_1 = \frac{\mu_1^\top \mu_*}{R^2}, \quad m_2 = \frac{\mu_2^\top \mu_*}{R^2}, \quad s = \frac{\mu_1^\top \mu_2}{R^2}. \quad (3.3)$$

For $c \in \{1, 2\}$, m_c represents the alignment of μ_c with the target modes $\pm \mu_*$, and s measures the alignment between the two student means. Crucially, the time evolution of these correlations recast the complex $2d$ -dimensional flow into a 3-dimensional ordinary differential equation:

$$\begin{aligned} \dot{m}_1 &= -\beta(t) \left[(m_2 - m_1 s) f(s, \beta(t)^{-\frac{1}{2}}) \right. \\ &\quad \left. + w_1 (1 - m_1^2) g(m_1, \beta(t)^{-\frac{1}{2}}) \right], \\ \dot{m}_2 &= -\beta(t) \left[(m_1 - m_2 s) f(s, \beta(t)^{-\frac{1}{2}}) \right. \\ &\quad \left. + w_2 (1 - m_2^2) g(m_2, \beta(t)^{-\frac{1}{2}}) \right], \\ \dot{s} &= -\beta(t) \left[2(1 - s^2) f(s, \beta(t)^{-\frac{1}{2}}) \right. \\ &\quad \left. + w_1 (m_2 - m_1 s) g(m_1, \beta(t)^{-\frac{1}{2}}) \right. \\ &\quad \left. + w_2 (m_1 - m_2 s) g(m_2, \beta(t)^{-\frac{1}{2}}) \right]. \end{aligned} \quad (3.4)$$

Detailed computations and expressions for f and g are given in Appendix C.2. Here, $f(s, \beta^{-1/2})$ represents the repulsive force arising from the student entropy term, while $g(m, \beta^{-1/2})$ encapsulates the attractive force from the cross-entropy term. The validity of the variance and gradient flow approximation are confirmed by the agreement of the numerical integration of eq. (3.4) with the SGD trajectories on both means and variances (fig. 3).

Notably, the above dynamical system does not depend on d , which only plays a role through the typical values of the summary statistics at initialization. In high dimensions, randomly initialized means concentrate

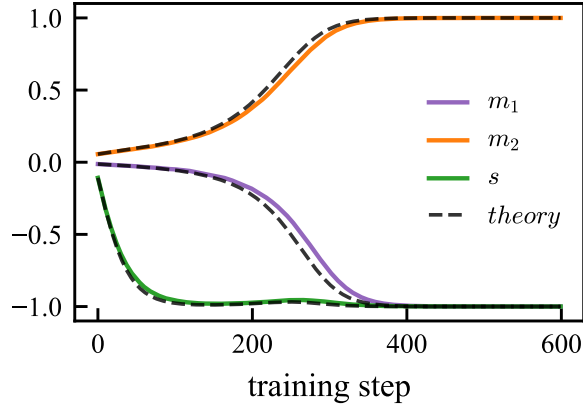


Figure 3: *Dynamics of the summary statistics.* Coloured curves correspond to SGD trajectories on both means and variances of the experiment corresponding to the third row of fig. 1. Black curves are the numerical integration of the eq. (3.4), that assume perfect gradient estimates and quasi static approximation for the variances $\sigma_{1,2}^2 = \beta(t)^{-1}$. Hyperparameters are $d = 512$, $R = 3$, and $w_* = 0.8$.

near the equator orthogonal to the target axis: $m_c \sim \mathcal{N}(0, 1/d)$, with a small overlap $s \sim \mathcal{N}(0, 1/d)$. To better understand the learning dynamics described in eq. (3.4) and the interplay with the dimension, we analyze two instructive limiting case of the dynamical system defined by the scaling of the temperature β^{-1} with respect to R^2 .

Remark 1. As $\beta(t)$ is a common factor in all equalities of eq. (3.4), it can be absorbed by a change of variable $t \rightarrow t' = \int_0^t dr \beta(r)$. ²

3.2 Limiting cases of the dynamics

The low *temperature regime* ($\beta \gg R^{-2}$) is observed in later stages of the annealing schedule. In Appendix C.3, we show that the cross-entropy term g dominates, while the entropic repulsion f vanishes exponentially:

$$f(s, \beta(t)^{-\frac{1}{2}}) \sim \frac{\sqrt{\pi}}{2} \frac{\sqrt{w_1 w_2}}{\sqrt{1-s}} \frac{1}{\sqrt{\beta R^2}} e^{-\frac{\beta R^2 (1-s)}{4}},$$

$$g(m, \beta(t)^{-\frac{1}{2}}) = -\tanh(R^2(m + \epsilon)) + \mathcal{O}\left(\frac{1}{\beta R^2}\right),$$

where the bias $\epsilon = \frac{1}{2R^2} \log \frac{w_*}{1-w_*}$ is an increasing function of w_* . Therefore, the evolution of the means according to eq. (3.4) becomes independent: $\dot{m}_c = w_c(1 - m_c^2) \tanh(R^2(m_c + \epsilon))$ for $c \in \{1, 2\}$. This creates two distinct basins of attraction for each mean separated by the hyperplane $m = -\epsilon$. The asymptotic fate of each mean is determined solely by whether its value at the onset of this regime is greater or lesser than $-\epsilon$.

A particular case is when no annealing is used ($\beta(t) = 1$, with a sufficiently large R), as in Soletskyi et al. (2025), which leads to inevitable mode collapse in high dimensional settings. If $1/\sqrt{d} \ll |\epsilon|$ (as in the preliminary experiments), the two student means will fall within the basin of attraction of the heaviest target mode with very high probability, resulting in mode collapse.

Instead, in the *high temperature* regime ($\beta \ll R^{-2}$), as discussed next, the student means are driven away from each other, and consequently, one of them escapes the basin of attraction of the heaviest mode.

²For the preliminary experiments, we adapted the learning rate as a function of $\beta(t)$: $\eta \mapsto \eta/\beta(t)$.

Namely, when the temperature is high, the entropy term dominates the cross-entropy term:

$$\begin{aligned} f(s, \beta(t)^{-\frac{1}{2}}) &= w_1 w_2 + \mathcal{O}(\beta R^2), \\ g(m, \beta(t)^{-\frac{1}{2}}) &= -\sqrt{\frac{2}{\pi}} \beta^{\frac{1}{2}} R(m + \epsilon) + \mathcal{O}(\beta R^2). \end{aligned} \quad (3.5)$$

Again, see Appendix C.3 for a detailed discussion. Here, the dynamics drive the overlap s to -1 , therefore effectively projecting the system onto the symmetric subspace where $\mu_1 = -\mu_2$ with both scaling as $1/\sqrt{d}$.

To analyze the stability of this configuration in high dimensions, we linearize the dynamics around the symmetric point ($s = -1$, $m_1 = -m_2 = 0$). The time evolution of the sum and difference of m_1 and m_2 decouple from s :

$$\begin{aligned} \dot{m}_1 + \dot{m}_2 &= - \left[2f(-1) + \frac{1}{2}g'(0) \right] (m_1 + m_2) - g(0), \\ \dot{m}_1 - \dot{m}_2 &= - \frac{1}{2}g'(0)(m_1 - m_2), \end{aligned} \quad (3.6)$$

where the second argument of f and g equal to $\beta^{-\frac{1}{2}}$ has been omitted for clarity. The system exhibits a saddle point structure. From the asymptotics of eq. (3.5), the sum is stable because $2f(-1) + \frac{1}{2}g'(0) \approx 2w_1 w_2 > 0$, however the difference is unstable since $g'(0) \approx -\sqrt{\frac{2}{\pi}} \beta^{\frac{1}{2}} R < 0$. The latter instability is the key mechanism to mitigate mode collapse as it drives m_1 and m_2 away from 0 and in opposite directions, each of the student mean specializing into a different target mode.

Interestingly, the escape speed from the saddle point $-g'(0) \propto R\sqrt{\beta}$ is a decreasing function of the temperature. This implies that arbitrarily high temperatures are comparatively less efficient at driving the specialization of the student means into different modes than temperatures closer (but still superior) to R^2 .

Leveraging this high-temperature dynamics, we derive next an analytical estimate for the probability of mode collapse.

3.3 Mode collapse probability

Mode collapse occurs if the student means have not been sufficiently driven away during the high temperature regime to fall into distinct basin of attraction of the low temperature regime. Assuming the transition from the high temperature regime to low temperature regime is sharp and occurs at inverse temperature $\beta = \alpha R^{-2}$ — where α is a constant of order 1 — yields the following mode collapse probability $p(\beta)$ for an annealing schedule β and random initialization of the student means:

$$p(\beta) = \int_{-2\epsilon e^{-I(\beta)}}^{2\epsilon e^{-I(\beta)}} dx \sqrt{\frac{d}{4\pi}} e^{-dx^2/4}, \quad (3.7)$$

where $I(\beta) = \int_0^{t_1} ds \sqrt{\frac{R^2 \beta(s)}{2\pi}}$ and t_1 is the transition time from the high to low temperature regime, defined implicitly by $\beta(t_1) = \alpha R^{-2}$. Details for the derivation of this estimate are provided in Appendix D. In particular, the exponential annealing schedule defined in eq. (2.4) yields

$$I(\beta_i, t_0) = \sqrt{\frac{2}{\pi}} \frac{t_0}{\log 1/\beta_i} (\sqrt{\alpha} - \sqrt{R^2 \beta_i}), \quad (3.8)$$

from which we compute a theoretical mode collapse probability that exhibits excellent agreement with the experimental results for $\alpha \approx 0.608$ (see isoprobability line of fig. 2 and fig. 7 in the Appendix). In the limit of high initial temperature $R^2 \beta_i \rightarrow 0$, the integral — and consequently the mode collapse probability — depends solely on the annealing rate β_i^{-1/t_0} . Namely, the probability scales as the inverse of the logarithm of the annealing rate: $I(\beta_i, t_0) \sim \sqrt{\frac{2}{\pi}} \frac{t_0}{\log 1/\beta_i}$. This implies that for sufficiently high initial temperatures, the annealing rate emerges as the relevant parameter to determine annealing success. Figure 5 confirms that this asymptotic behavior is already at play in the preliminary experiments: as the initial temperature increases,

the curves rapidly converge toward this asymptotic regime where the mode collapse probability is dictated purely by the annealing rate.

The success of annealing depends on maximizing the integral $I(\beta_i, t_0)$, which has one global maximum (more details in Appendix section D.3). Important deviation from this optimum leads to failure in two different ways. If the initial temperature is set too low ($\beta_i > \beta_i^*$), the duration of the high-temperature regime is too short to generate sufficient mode separation and prevent collapse. Conversely, for a fixed annealing time t_0 , raising the initial temperature ($\beta_i < \beta_i^*$) can end up being detrimental because the integrand — equal to the escape speed $\sqrt{R^2\beta(s)}$ — remains negligible for a comparatively longer time. Consequently, when the true mode separation R is unknown, the most robust strategy for tuning the annealing schedule is to scale t_0 and β_i in successive trials in a way that ensures that the annealing rate is not increasing.

4 Numerical experiments with normalizing flows

4.1 Experimental setup

In this section, we validate our theoretical findings in a practical setting by learning a multimodal target using a highly expressive variational family: RealNVPs normalizing flows Dinh et al. (2017). While generative models like RealNVPs offer significant flexibility, high expressivity alone does not resolve mode collapse for multimodal targets. Consequently, annealing is an increasingly common strategy for mitigating it in practice.

To isolate the influence of the annealing schedule, we retain the bimodal Gaussian target distribution (Equation 2.1) in dimension $d = 128$ and employ the exponential annealing schedule defined in eq. (2.4). The student distribution q_θ is parameterized using a RealNVP.

A normalizing flow defines a parametric invertible map $\Phi_\theta : \mathbb{R}^d \rightarrow \mathbb{R}^d$ with a tractable Jacobian, optimized to transport samples from a base distribution ρ_0 to the target π . In this implementation, we employ a standard Gaussian base distribution $\rho_0(z) = \mathcal{N}(0, I_d)$ in dimension $d = 128$. Our RealNVP architecture consists of 8 affine coupling layers. The internal scale and translation networks within each coupling block are multi-layer perceptrons (MLPs) with 4 hidden layers and a hidden dimension of $4d = 512$.

The target modes are separated by $R = 3$ with the weight imbalance $w_* = 0.8$. Using the change of variable formula, the loss is estimated as a Monte Carlo estimator of:

$$\mathcal{L}(\theta, \beta) = \int_{\mathbb{R}^d} dz \rho_0(z) \log \left[\frac{\rho_0(z) \left| \det \frac{\partial \Phi_\theta}{\partial z}(z) \right|^{-1}}{\pi(\Phi_\theta(z))^\beta} \right].$$

Unlike the setting of a Gaussian mixture student, where the overlap s serves as a direct order parameter, detecting mode collapse in high-dimensional flows requires a derived metric. We utilize the variance of the generated samples projected onto $\hat{\mu} = \mu_* / R$. Specifically, we monitor $\mathcal{V} = \text{Var}_{x \sim q_\theta}[x \cdot \hat{\mu}]$. A collapsed model capturing only a single mode (variance ≈ 1) yields $\mathcal{V} \approx 1$, whereas a model that correctly learns the target mixture yields a significantly higher variance ($\mathcal{V} \approx 2.6$ for our parameters). Accordingly, we define a collapse threshold of $\mathcal{V} < 1.6$.

4.2 Results

Figure 4 reports the probability of mode collapse across a grid of initial temperatures β_i and annealing times t_0 . The results exhibit the same phenomenology observed in the Gaussian mixture student analysis (fig. 2). If the initial temperature is too low (high β_i) or no annealing is applied, mode collapse is inevitable regardless of the model’s expressivity. For a fixed computational budget (fixed t_0), there exists an optimal initial temperature that maximizes the probability of success; increasing the temperature beyond this point becomes detrimental, as the annealing rate becomes too fast to resolve mode collapse. Moreover, fig. 5 confirms that for sufficiently high initial temperatures, the mode collapse probability depends essentially on the annealing rate alone. This recovers for a complex generative model architecture a behavior predicted by our theoretical analysis, which further confirms the relevance of our theoretical insights in practical settings.

These results are of interest for practitioners dealing with multimodal targets, even when the mode separation R is unknown. To reliably enter the mode collapse mitigation parameter region, one cannot simply increase the initial temperature indefinitely. Instead, our findings indicate that a better strategy

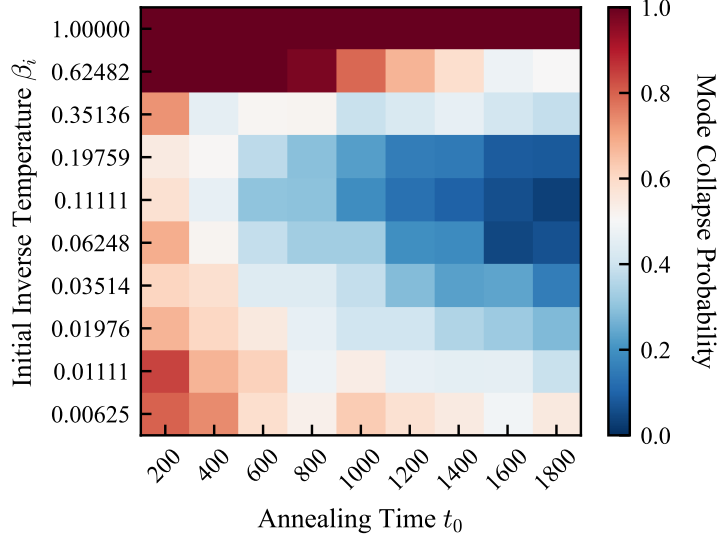


Figure 4: *Annealed VI mode collapse probability with RealNVP student.* Mode collapse probabilities are computed on 200 different runs for each β_i and annealing time t_0 . We employ an exponential annealing schedule (eq. (2.4)) on a bimodal Gaussian mixture target with hyperparameters $d = 128$, $R = 3$ and $w_* = 0.8$. The generative model is a RealNVP with 8 coupling layers, each containing two MLPs of depth 4 and hidden dimension $4d = 512$.

is to increase the annealing duration t_0 alongside the initial temperature, ensuring that the annealing rate remains sufficiently small to resolve the modes.

5 Conclusion

In this work, we have presented a theoretical investigation of annealing in VI on bimodal Gaussian mixture target distribution. Based on a low dimensional description of the gradient flow dynamics and a quasi-static approximation for the variances, we show that simulated annealing can robustly mitigate mode collapse by controlling the balance between the entropy and cross-entropy terms of the reversed Kullback-Leibler divergence. Characterizing the interplay between initial temperature and annealing time, we show that an increase in the initial temperature should be accompanied by an increase in the annealing time when searching for a combination avoiding mode collapse. Our numerical experiments show that this strategy works with more practical variational families such as RealNVPs. Overall, our theoretical findings, in agreement with our numerical observations, highlight the role of the annealing rate that controls the probability of mode collapse when starting at high enough temperature.

Perspectives of interest for this work include the study of multimodal targets with more than two modes and variational family with a number of modes not matching the number of the target modes. Another, interesting direction is to replicate this study for VI with diffusion models, a recent promising framework [Tzen and Raginsky \(2019\)](#); [Zhang and Chen \(2021\)](#); [Vargas et al. \(2023\)](#); [Richter and Berner \(2023\)](#); [Phillips et al. \(2024\)](#); [Noble et al. \(2025\)](#). In this approach, VI is performed on a path measure space which maybe more robust to mode collapse.

Data availability

A running implementation of the algorithms and all code to reproduce results presented in this work are publicly available at https://github.com/Luijios/annealed_vi_gmms.

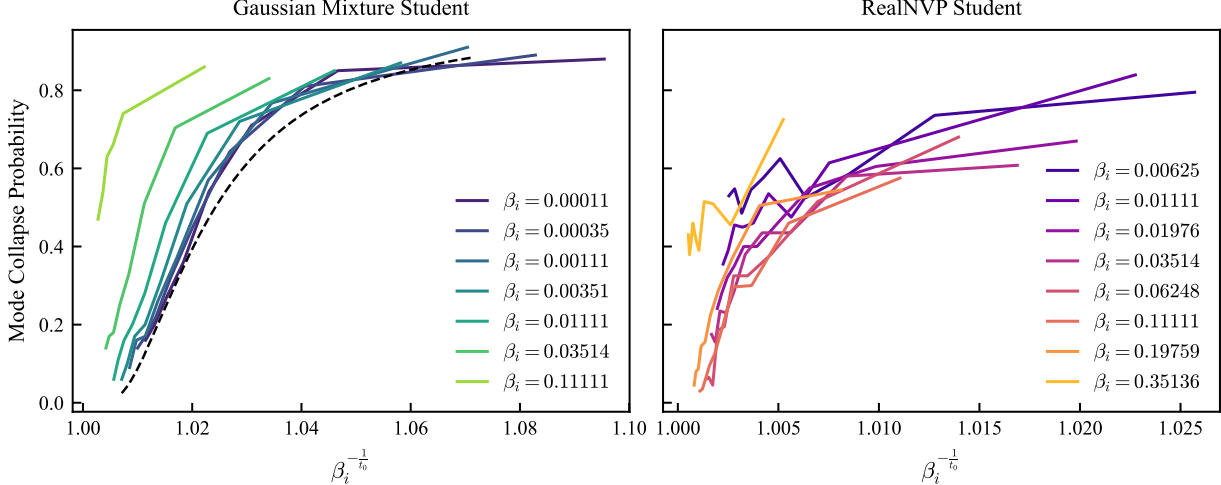


Figure 5: *Probability of mode collapse as a function of the annealing rate β_i^{-1/t_0} , for an exponential annealing schedule given by eq. (2.4).* For the Gaussian mixture student the data are the same as fig. 2, hyperparameters are $d = 512, R = 3, w_* = 0.8$. The dashed black line is the high initial temperature ($\beta_i \rightarrow 0$) asymptote of the mode collapse probability eq. (3.7) ($\alpha = 0.608$). For the realNVP student the data are the same as fig. 4, hyperparameters are $d = 128, R = 3, w_* = 0.8$.

Acknowledgements

This work was supported by the PR[AI]RIE-PSAI project, a French government grant managed by the Agence Nationale de la Recherche under the France 2030 program, reference ANR-23-IACL-0008. BL also acknowledges funding from the Choose France - CNRS AI Rising Talents program.

References

- M. S. Albergo, G. Kanwar, and P. E. Shanahan. Flow-based generative models for Markov chain Monte Carlo in lattice field theory. *Physical Review D*, 100(3):034515, Aug. 2019. ISSN 2470-0010, 2470-0029. doi: 10.1103/PhysRevD.100.034515. arXiv:1904.12072 [hep-lat].
- A. Barzegar, F. Hamze, C. Amey, and J. Machta. Optimal schedules for annealing algorithms. *Physical Review E*, 109(6):065301, June 2024. doi: 10.1103/PhysRevE.109.065301.
- D. M. Blei, A. Kucukelbir, and J. D. McAuliffe. Variational Inference: A Review for Statisticians. *Journal of the American Statistical Association*, 112(518):859–877, Apr. 2017. ISSN 0162-1459, 1537-274X. doi: 10.1080/01621459.2017.1285773.
- D. Blessing, X. Jia, J. Esslinger, F. Vargas, and G. Neumann. Beyond elbos: a large-scale evaluation of variational methods for sampling. In *Proceedings of the 41st International Conference on Machine Learning*, ICML’24. JMLR.org, 2024.
- L. Dinh, J. Sohl-Dickstein, and S. Bengio. Density estimation using real NVP. In *5th International Conference on Learning Representations, ICLR 2017, Toulon, France, April 24–26, 2017, Conference Track Proceedings*. OpenReview.net, 2017. URL <https://openreview.net/forum?id=HkpbnH9lx>.
- L. Grenioux, M. Noble, and M. Gabré. Improving the evaluation of samplers on multi-modal targets. In *ICLR Workshop on Frontiers in Probabilistic Inference: Learning Meets Sampling*, Apr. 2025.

D. C. Hackett, C.-C. Hsieh, M. S. Albergo, D. Boyda, J.-W. Chen, K.-F. Chen, K. Cranmer, G. Kanwar, and P. E. Shanahan. Flow-based sampling for multimodal distributions in lattice field theory, July 2021.

B. Hajek. Cooling schedules for optimal annealing. *Mathematics of Operations Research*, 13(2):311–329, 1988. ISSN 0364765X, 15265471. URL <http://www.jstor.org/stable/3689827>.

M. Hibat-Allah, E. M. Inack, R. Wiersema, R. G. Melko, and J. Carrasquilla. Variational Neural Annealing. *Nature Machine Intelligence*, 3(11):952–961, Oct. 2021. ISSN 2522-5839. doi: 10.1038/s42256-021-00401-3. arXiv:2101.10154 [cond-mat].

C.-W. Huang, S. Tan, A. Lacoste, and A. C. Courville. Improving Explorability in Variational Inference with Annealed Variational Objectives. In *Advances in Neural Information Processing Systems*, volume 31. Curran Associates, Inc., 2018.

T. Huix, A. Korba, A. O. Durmus, and E. Moulines. Theoretical Guarantees for Variational Inference with Fixed-Variance Mixture of Gaussians. In *Proceedings of the 41st International Conference on Machine Learning*, pages 20700–20721. PMLR, July 2024. URL <https://proceedings.mlr.press/v235/huix24a.html>. ISSN: 2640-3498.

M. I. Jordan, Z. Ghahramani, T. S. Jaakkola, and L. K. Saul. An Introduction to Variational Methods for Graphical Models. *Machine Learning*, 37(2):183–233, Nov. 1999. ISSN 1573-0565. doi: 10.1023/A:1007665907178.

R. Jordan, D. Kinderlehrer, and F. Otto. The variational formulation of the fokker–planck equation. *SIAM Journal on Mathematical Analysis*, 29(1):1–17, 1998. doi: 10.1137/S0036141096303359. URL <https://doi.org/10.1137/S0036141096303359>.

S. A. Khandoker, E. M. Inack, and M. Hibat-Allah. Lattice protein folding with variational annealing. *Machine Learning: Science and Technology*, 6(3):035023, Aug. 2025. ISSN 2632-2153. doi: 10.1088/2632-2153/adf376.

T. LeMinh, J. Arbel, T. Möllenhoff, M. E. Khan, and F. Forbes. Natural variational annealing for multimodal optimization. *arXiv preprint arXiv:2501.04667*, 2025.

T. Minka. Divergence measures and message passing. Technical Report MSR-TR-2005-173, Technical report, Microsoft Research, 2005.

W. Nadler and U. H. E. Hansmann. Dynamics and optimal number of replicas in parallel tempering simulations. *Physical Review E*, 76(6):065701, Dec. 2007. doi: 10.1103/PhysRevE.76.065701.

K. A. Nicoli, C. J. Anders, T. Hartung, K. Jansen, P. Kessel, and S. Nakajima. Detecting and mitigating mode-collapse for flow-based sampling of lattice field theories. *Physical Review D*, 108(11):114501, Dec. 2023. doi: 10.1103/PhysRevD.108.114501.

M. Noble, L. Grenioux, M. Gabré, and A. O. Durmus. Learned Reference-based Diffusion Sampler for multi-modal distributions. In *The Thirteenth International Conference on Learning Representations*, Apr. 2025.

F. Noé, S. Olsson, J. Köhler, and H. Wu. Boltzmann generators: Sampling equilibrium states of many-body systems with deep learning. *Science*, 365(6457):eaaw1147, Sept. 2019. ISSN 0036-8075, 1095-9203. doi: 10.1126/science.aaw1147.

M. Petit-Talamon, M. Lambert, and A. Korba. Variational Inference with Mixtures of Isotropic Gaussians. In *The Thirty-ninth Annual Conference on Neural Information Processing Systems*, Oct. 2025.

A. Phillips, H.-D. Dau, M. J. Hutchinson, V. D. Bortoli, G. Deligiannidis, and A. Doucet. Particle Denoising Diffusion Sampler. In *Proceedings of the 41st International Conference on Machine Learning*, pages 40688–40724. PMLR, July 2024.

D. Rezende and S. Mohamed. Variational Inference with Normalizing Flows. In *Proceedings of the 32nd International Conference on Machine Learning*, pages 1530–1538. PMLR, June 2015.

L. Richter and J. Berner. Improved sampling via learned diffusions. In *The Twelfth International Conference on Learning Representations*, Oct. 2023.

D. Saad and S. Solla. Dynamics of on-line gradient descent learning for multilayer neural networks. *Advances in neural information processing systems*, 8, 1995.

H. Schopmans and P. Friederich. Temperature-Annealed Boltzmann Generators. In *Forty-Second International Conference on Machine Learning*, June 2025.

R. Soletskyi, M. Gabré, and B. Loureiro. A theoretical perspective on mode collapse in variational inference. *Machine Learning: Science and Technology*, 6(2):025056, June 2025. ISSN 2632-2153. doi: 10.1088/2632-2153/adde2a.

S. Syed, V. Romaniello, T. Campbell, and A. Bouchard-Cote. Parallel tempering on optimized paths. In *Proceedings of the 38th International Conference on Machine Learning*, pages 10033–10042. PMLR, July 2021.

B. Tzen and M. Raginsky. Theoretical guarantees for sampling and inference in generative models with latent diffusions. In *Proceedings of the Thirty-Second Conference on Learning Theory*, pages 3084–3114. PMLR, June 2019.

L. Vaitl, K. A. Nicoli, S. Nakajima, and P. Kessel. Gradients should stay on path: Better estimators of the reverse- and forward KL divergence for normalizing flows. *Machine Learning: Science and Technology*, 3(4):045006, Dec. 2022. ISSN 2632-2153. doi: 10.1088/2632-2153/ac9455.

F. Vargas, W. S. Grathwohl, and A. Doucet. Denoising Diffusion Samplers. In *The Eleventh International Conference on Learning Representations*, Sept. 2023.

Y. Wang, C. Chi, and A. R. Dinner. Mitigating mode collapse in normalizing flows by annealing with an adaptive schedule: Application to parameter estimation. *arXiv preprint arXiv:2505.03652*, 2025.

P. Weiss. L’hypothèse du champ moléculaire et la propriété ferromagnétique. *Journal de Physique Théorique et Appliquée*, 6(1):661–690, 1907. ISSN 0368-3893. doi: 10.1051/jphystab:019070060066100.

D. Wu, L. Wang, and P. Zhang. Solving Statistical Mechanics Using Variational Autoregressive Networks. *Physical Review Letters*, 122(8):080602, Feb. 2019. ISSN 0031-9007, 1079-7114. doi: 10.1103/PhysRevLett.122.080602. arXiv:1809.10606 [cond-mat].

Q. Zhang and Y. Chen. Path Integral Sampler: A Stochastic Control Approach For Sampling. In *International Conference on Learning Representations*, Oct. 2021.

First, we recall the general context of Variational Inference. Given a potentially unnormalized target probability distribution π on \mathbb{R}^d , and a parametric probability distribution q_θ , the goal is to minimize the reverse Kullback-Leibler objective $\mathcal{D}_{KL}(q_\theta||\pi)$ with respect to θ . In other words, the goal is to find:

$$\theta_* = \operatorname{argmin}_{\theta \in \Theta} \{\mathcal{D}_{KL}(q_\theta||\pi)\}. \quad (1)$$

In order to do so, a common strategy is annealing. Introducing an inverse temperature $\beta < 1$, the goal is to relax the objective by minimizing $\mathcal{D}_{KL}(q_\theta||\pi^\beta)$. The inverse temperature is then progressively increased to the target value $\beta = 1$.

Here we considered for q_θ either isotropic Gaussian mixtures, or the probability distribution of a RealNVP normalizing flow. For uniform-weighted Gaussian mixtures,

$$q_\theta = \sum_{i=1}^K \frac{1}{K} \mathcal{N}(\mu_i, \sigma_i^2 I_d), \quad (2)$$

where $\theta = (\mu_1, \dots, \mu_K, \sigma_1, \dots, \sigma_K) \in \mathbb{R}^{K(d+1)}$. In the following section we describe the update rule used to optimize θ .

A JKO scheme for isotropic Gaussian mixtures

In numerical experiments with Gaussian mixtures, we use a JKO scheme [Jordan et al. \(1998\)](#) with a Wasserstein distance adapted to isotropic Gaussians mixtures that has beein introduced by [Petit-Talamon et al. \(2025\)](#). It results in the following update rules:

$$\mu_{t+1} = \mu_t - \eta \nabla_{\mu_t} \mathcal{D}_{KL}(q_{\theta_t}||\pi^\beta) \quad (A.1)$$

$$\sigma_{t+1}^2 = \left(1 - \frac{2\eta}{d} \nabla_{\sigma_t^2} \mathcal{D}_{KL}(q_{\theta_t}||\pi^\beta)\right)^2 \sigma_t^2. \quad (A.2)$$

This update rule is equivalent to standard gradient descent update on μ_t and σ_t (not σ_t^2) with a specific scaling between the learning rate of the means and the learning rate of the standard deviations. In fact:

$$\begin{aligned} \sigma_{t+1} &= \left(1 - \frac{2\eta}{d} \nabla_{\sigma_t^2} \mathcal{D}_{KL}(q_{\theta_t}||\pi^\beta)\right) \sigma_t \\ &= \sigma_t - \frac{\eta}{d} 2\sigma_t \nabla_{\sigma_t^2} \mathcal{D}_{KL}(q_{\theta_t}||\pi^\beta) = \sigma_t - \frac{\eta}{d} \nabla_{\sigma_t} \mathcal{D}_{KL}(q_{\theta_t}||\pi^\beta). \end{aligned} \quad (A.3)$$

In the notations of the main body, this implies $\eta_\sigma = \eta_\mu/d$ with the following update rule:

$$\theta_{t+1} = \theta_t - \eta_\theta \nabla_{\theta_t} \mathcal{D}_{KL}(q_{\theta_t}||\pi^\beta) \quad (A.4)$$

B Additional preliminary experiments

fig. 6 completes fig. 1 and illustrates additional learning strategies. Initial student means are the same as the one of fig. 1. Frozen variances (first row) lead to mode collapse, even if the variance is set to $1/10R^2$.

Interestingly, the variances rapidly converge to the target value of 1 even if we freeze the means (second row), which further motivates the quasi-static assumption for the variances that we employ on the means in the analytical analysis.

C Gradient flow dynamics and low dimensional dynamical system

In the following, we derive the analytical description of annealed Variational Inference with bimodal Gaussians. By definition, the reverse KL divergence between an isotropic Gaussian mixture with K components

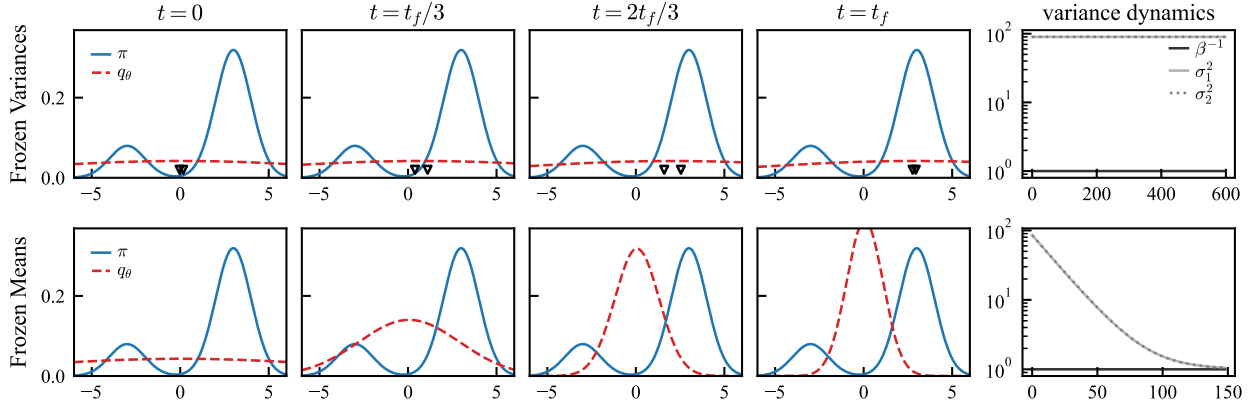


Figure 6: *Additional preliminary experiments.* The first 4 columns show the marginal density along the direction of μ_* of both π and q_θ , at 4 different training stages. The fifth column shows the variance dynamics. Each row represents a different scenario; from top to bottom: non learned variances with $\sigma_{1,2}^2 = 1/10R^2$ fixed, non learned means with $\sigma_{1,2}^2$ initialized to $1/10R^2$. Black triangles on the first row indicate the projection of $\mu_{1,2}$ along the axis of μ_* . Hyperparameters are: $d = 512, R = 3, w_* = 0.8, w_1 = 0.5$ and learning rate $\eta = 0.05$.

and an arbitrary target distribution π at inverse temperature β is:

$$\mathcal{D}_{KL}(q_\theta || \pi^\beta) = \sum_{i=1}^K \frac{1}{K} \int_{\mathbb{R}^d} dx \frac{e^{-(x-\mu_i)^2/2\sigma_i^2}}{(2\pi\sigma_i^2)^{d/2}} \log \left(\frac{\sum_{j=1}^K \frac{1}{K} \frac{e^{-(x-\mu_j)^2/2\sigma_j^2}}{(2\pi\sigma_j^2)^{d/2}}}{\pi(x)^\beta} \right). \quad (\text{C.1})$$

The goal of this section is to study the gradient flow dynamics related to this loss:

$$\dot{\theta} = -\eta_\theta \nabla_\theta \mathcal{D}_{KL}(q_\theta || \pi^\beta), \quad (\text{C.2})$$

in the particular case when q_θ and π are bimodal gaussian mixtures.

$$\pi(x) = w_* \mathcal{N}(x|\mu_*, I_d) + (1-w_*) \mathcal{N}(x|\mu_*, I_d) \quad (\text{C.3})$$

$$q_\theta(x) = w_1 \mathcal{N}(x|\mu_1, \sigma_1^2 I_d) + (1-w_1) \mathcal{N}(x|\mu_2, \sigma_2^2 I_d) \quad (\text{C.4})$$

In what will follow, we motivate the simplifying quasi-static assumption made on the variance $\sigma_1^2 = \sigma_2^2 = \beta^{-1}$.

C.1 On the variance dynamics

Let's try first to compute the derivative of the loss with respect to σ_1 :

$$\begin{aligned} \frac{\partial \mathcal{D}_{KL}}{\partial \sigma_1} = & -\frac{w_1 d}{\sigma_1} \mathbf{E}_x \left[\frac{w_1}{w_1 + w_2 (\frac{\sigma_1}{\sigma_2})^d e^{-(\sigma_1 x + \mu_1 - \mu_2)^2 / 2\sigma_2^2 + x^2 / 2}} \right] \\ & + w_1 d\sigma_1 \\ & - \beta w_1 R \mathbf{E}_x \left[x \frac{w_* e^{R^2 m_1 + \sigma_1 R x} - (1 - w_*) e^{-R^2 m_1 - \sigma_1 R x}}{w_* e^{R^2 m_1 + \sigma_1 R x} + (1 - w_*) e^{-R^2 m_1 - \sigma_1 R x}} \right] \\ & + w_2 \mathbf{E}_x \left[\frac{-dw_1/\sigma_1 + w_1/\sigma_1^3 (\sigma_2 x + \mu_2 - \mu_1)^2}{w_1 + w_2 (\frac{\sigma_1}{\sigma_2})^d e^{(\sigma_1 x + \mu_1 - \mu_2)^2 / 2\sigma_2^2 - x^2 / 2}} \right] \\ & - w_1 \mathbf{E}_x \left[\frac{w_2 x (\sigma_1 x + \mu_1 - \mu_2) / \sigma_2^2}{w_1 (\frac{\sigma_2}{\sigma_1})^d e^{(\sigma_1 x + \mu_1 - \mu_2)^2 / 2\sigma_2^2 - x^2 / 2} + w_2} \right]. \end{aligned} \quad (\text{C.5})$$

This equation is untractable. However in practice, the variances closely track the temperature: $\sigma_1^2 \approx \sigma_2^2 \approx \beta^{-1}$ as shown by fig. 1. This motivates the quasi-static approximation that we use for the analytical derivations that will follow.

$$\sigma_1^2(t) = \sigma_2^2(t) = \beta^{-1}(t) \quad (\text{C.6})$$

This approximation might be counter-intuitive at first, because it do not depend on the value of the means. Here we present an argument providing some intuition on the behavior of the variance in a simple setting. For this paragraph only, we consider isotropic Gaussians: $q_\theta = \mathcal{N}(\mu, \sigma^2 I_d)$, $\pi = \mathcal{N}(0, I_d)$. Then the reverse KL divergence is equal to:

$$\mathcal{D}_{KL}(q_\theta || \pi^\beta) = -\frac{d}{2} \log(2\pi e \sigma^2) + \beta \frac{d\sigma^2}{2} + \beta \frac{\mu^2}{2} + \beta \frac{d}{2} \log(2\pi). \quad (\text{C.7})$$

Regardless of μ , the value of σ^2 that minimizes the loss is $\sigma^2 = \beta^{-1}$. We believe that this observation might extend to the bimodal case.

C.2 Gradient flow equation for the means

In this section we derive the learning dynamics of the means presented in the analytical analysis section of the main body. As a preliminary, we need to compute and simplify $\mathcal{D}_{KL}(q_\theta || \pi^\beta)$ when q_θ is a Gaussian mixture of the form eq. (2), in the particular case of *equal variances*: $\sigma = \sigma_1 = \dots = \sigma_K$. — We restrict to this case since we will eventually consider a quasi-static approximations on the variances $\sigma_i = \beta^{-1}$. — The loss simplifies :

$$\mathcal{D}_{KL}(q_\theta || \pi^\beta) = -\frac{d}{2} \log(2\pi e \sigma^2) + \int_{\mathbb{R}^d} dx \frac{e^{-x^2/2}}{(2\pi)^{d/2}} \sum_i \frac{1}{K} \log \left(\sum_{j=1}^K \frac{1}{K} e^{-\frac{x^T (\mu_i - \mu_j)}{\sigma} - \frac{|\mu_i - \mu_j|^2}{2\sigma^2}} \right) \quad (\text{C.8})$$

$$- \beta \int_{\mathbb{R}^d} dx \frac{e^{-x^2/2}}{(2\pi)^{d/2}} \sum_i \frac{1}{K} \log(\pi(\sigma x + \mu_i)). \quad (\text{C.9})$$

$$(\text{C.10})$$

Now, we set $K = 2$ and π as a bimodal isotropic Gaussian mixture and use notations of eq. (2.1). We fix the separation radius $|\mu_*| = R$ and the radii of the student means $= |\mu_k|$. This yields:

$$\mathcal{D}_{KL}(q_\theta || \pi^\beta) = -\frac{d}{2} \log(2\pi e \sigma^2) - \frac{R^2}{\sigma^2} + \int_{\mathbb{R}^d} dx \frac{e^{-x^2/2}}{(2\pi)^{d/2}} \sum_{i=1}^2 w_i \log \left(\sum_{j=1}^2 w_j e^{\frac{x^T \mu_j}{\sigma} + \frac{\mu_i^T \mu_j}{\sigma^2}} \right) \quad (\text{C.11})$$

$$+ \beta \frac{d\sigma^2}{2} - \beta \int_{\mathbb{R}^d} dx \frac{e^{-x^2/2}}{(2\pi)^{d/2}} \sum_{i=1}^2 w_i \log \left(w_* e^{(\sigma x + \mu_i) \mu_*} + (1 - w_*) e^{-(\sigma x + \mu_i) \mu_*} \right) \quad (\text{C.12})$$

up to an additional constant that does not depend on μ_i nor on σ . Note that the loss only depends on the vectors $\mu_*, \mu_{1,2}$ through the following statistics:

$$m_i = \frac{\mu_i \cdot \mu_x}{R^2}, \quad s = \frac{\mu_1 \cdot \mu_2}{R^2}. \quad (\text{C.13})$$

In the following, we alleviate notations by replacing $\int_{\mathbb{R}^d} dx \frac{e^{-x^2/2}}{(2\pi)^{d/2}} [\dots]$ with $\mathbb{E}_{x \sim \mathcal{N}(0, I_d)} [\dots]$

Let's first compute the dynamics of the means. By definition, the spherical gradient flow is given by:

$$\dot{\mu}_c(t) = \left(I_d - \frac{\mu_c(t) \mu_c(t)^T}{R^2} \right) \nabla_{\mu_c} \mathcal{L}(\theta(t), \beta(t)) \quad c = 1, 2. \quad (\text{C.14})$$

Let's first compute the Euclidean gradient of the loss eq. (C.12) with respect to $\mu_{1,2}$.

$$\begin{aligned} \nabla_{\mu_1} \mathcal{D}_{KL} &= w_1 \mathbb{E}_{x \sim \mathcal{N}(0, I_d)} \left[\frac{1}{\sigma} \frac{w_1(x + 2\frac{\mu_1}{\sigma})e^{(x + \frac{\mu_1}{\sigma}) \cdot \frac{\mu_1}{\sigma}} + w_2 \frac{\mu_2}{\sigma} e^{(x + \frac{\mu_1}{\sigma}) \cdot \frac{\mu_2}{\sigma}}}{w_1 e^{(x + \frac{\mu_1}{\sigma}) \cdot \frac{\mu_1}{\sigma}} + w_2 e^{(x + \frac{\mu_1}{\sigma}) \cdot \frac{\mu_2}{\sigma}}} \right] \\ &\quad + w_2 \mathbb{E}_{x \sim \mathcal{N}(0, I_d)} \left[\frac{1}{\sigma} \frac{w_1(x + \frac{\mu_2}{\sigma})e^{(x + \frac{\mu_2}{\sigma}) \cdot \frac{\mu_1}{\sigma}}}{w_1 e^{(x + \frac{\mu_2}{\sigma}) \cdot \frac{\mu_1}{\sigma}} + w_2 e^{(x + \frac{\mu_2}{\sigma}) \cdot \frac{\mu_2}{\sigma}}} \right] \\ &\quad - \beta w_1 \mathbb{E}_{x \sim \mathcal{N}(0, I_d)} \left[\frac{w_* \mu_* e^{(\sigma x + \mu_1) \cdot \mu_*} - (1 - w_*) \mu_* e^{-(\sigma x + \mu_1) \cdot \mu_*}}{w_* e^{(\sigma x + \mu_1) \cdot \mu_*} + (1 - w_*) e^{-(\sigma x + \mu_1) \cdot \mu_*}} \right] \end{aligned} \quad (\text{C.15})$$

Defining the sigmoid function $\text{expit}(t) = (1 + e^{-t})^{-1}$, we can rewrite:

$$\begin{aligned} \nabla_{\mu_1} \mathcal{D}_{KL} &= \frac{w_1}{\sigma} \mathbb{E}_{x \sim \mathcal{N}(0, I_d)} \left[(x + 2\frac{\mu_1}{\sigma}) \text{expit} \left((\frac{\mu_1}{\sigma} - \frac{\mu_2}{\sigma}) \cdot (x + \frac{\mu_1}{\sigma}) + \log \frac{w_1}{w_2} \right) \right. \\ &\quad \left. + \frac{\mu_2}{\sigma} \text{expit} \left((\frac{\mu_2}{\sigma} - \frac{\mu_1}{\sigma}) \cdot (x + \frac{\mu_1}{\sigma}) + \log \frac{w_2}{w_1} \right) \right] \\ &\quad + \frac{w_2}{\sigma} \mathbb{E}_{z \sim \mathcal{N}(0, I_d)} \left[(x + \frac{\mu_2}{\sigma}) \text{expit} \left((\frac{\mu_1}{\sigma} - \frac{\mu_2}{\sigma}) \cdot (x + \frac{\mu_2}{\sigma}) + \log \frac{w_1}{w_2} \right) \right] \\ &\quad + \beta w_1 \mathbb{E}_{z \sim \mathcal{N}(0, I_d)} \left[\mu_* \left(1 - 2 \text{expit} \left(2\mu_* \cdot (\sigma x + \mu_1) + \log \frac{w_*}{1 - w_*} \right) \right) \right] \end{aligned} \quad (\text{C.16})$$

It's convenient to eliminate $xg(x)$ -like terms using Stein's lemma. Since $x \sim \mathcal{N}(0, I_d)$, we have $\mathbb{E}_x[xg(x)] = \mathbb{E}_x[\nabla g(x)]$, and:

$$\begin{aligned} \nabla_{\mu_1} \mathcal{D}_{KL} &= w_1 \mathbb{E}_{x \sim \mathcal{N}(0, I_d)} \left[\frac{\mu_1}{\sigma^2} \text{expit} \left((\frac{\mu_1}{\sigma} - \frac{\mu_2}{\sigma}) \cdot (x + \frac{\mu_1}{\sigma}) + \log \frac{w_1}{w_2} \right) \left(3 - \text{expit} \left((\frac{\mu_1}{\sigma} - \frac{\mu_2}{\sigma}) \cdot (x + \frac{\mu_1}{\sigma}) + \log \frac{w_1}{w_2} \right) \right) \right. \\ &\quad \left. + \frac{\mu_2}{\sigma^2} \text{expit} \left((\frac{\mu_2}{\sigma} - \frac{\mu_1}{\sigma}) \cdot (x + \frac{\mu_1}{\sigma}) + \log \frac{w_2}{w_1} \right)^2 + \beta \mu_* \left(1 - 2 \text{expit} \left(2\mu_* \cdot (\sigma x + \mu_1) + \log \frac{w_*}{1 - w_*} \right) \right) \right] \\ &\quad + w_2 \mathbb{E}_{x \sim \mathcal{N}(0, I_d)} \left[\frac{\mu_1}{\sigma^2} \text{expit} \left((\frac{\mu_1}{\sigma} - \frac{\mu_2}{\sigma}) \cdot (x + \frac{\mu_2}{\sigma}) + \log \frac{w_1}{w_2} \right) \left(1 - \text{expit} \left((\frac{\mu_1}{\sigma} - \frac{\mu_2}{\sigma}) \cdot (x + \frac{\mu_2}{\sigma}) + \log \frac{w_1}{w_2} \right) \right) \right. \\ &\quad \left. + \frac{\mu_2}{\sigma^2} \text{expit} \left((\frac{\mu_1}{\sigma} - \frac{\mu_2}{\sigma}) \cdot (x + \frac{\mu_2}{\sigma}) + \log \frac{w_1}{w_2} \right)^2 \right] \end{aligned} \quad (\text{C.17})$$

Projecting the gradient with eq. (3.2) results in:

$$\begin{aligned} \nabla_{\mu_1}^S \mathcal{D}_{KL} &= \frac{\mu_2 - \mu_1 s}{\sigma^2} \mathbb{E}_{x \sim \mathcal{N}(0, I_d)} \left[w_1 \text{expit} \left((\frac{\mu_2}{\sigma} - \frac{\mu_1}{\sigma}) \cdot (x + \frac{\mu_1}{\sigma}) + \log \frac{w_2}{w_1} \right) \right. \\ &\quad \left. + w_2 \text{expit} \left((\frac{\mu_1}{\sigma} - \frac{\mu_2}{\sigma}) \cdot (x + \frac{\mu_2}{\sigma}) + \log \frac{w_1}{w_2} \right)^2 \right] \\ &\quad + \beta w_1 (\mu_* - m_1 \mu_1) \mathbb{E}_{x \sim \mathcal{N}(0, I_d)} \left[1 - 2 \text{expit} \left(2\mu_* \cdot (\sigma x + \mu_1) + \log \frac{w_*}{1 - w_*} \right) \right]. \end{aligned} \quad (\text{C.18})$$

We notice that the functions inside the expectations depend only on the projections of x in the direction of two axis: $\mu_* \cdot x$ which has variance R^2 , and $(\mu_2 - \mu_1) \cdot x$ which has variance $2R^2(1-s)$.

Introducing the functions:

$$\begin{aligned} f(s, \sigma) &= \mathbb{E}_{x \sim \mathcal{N}(0,1)} \left[w_1 \text{expit} \left(\frac{R}{\sigma} \sqrt{2(1-s)} x + \frac{R^2}{\sigma^2} (s-1) + \log \frac{w_2}{w_1} \right)^2 + w_2 \text{expit} \left(\frac{R}{\sigma} \sqrt{2(1-s)} x + \frac{R^2}{\sigma^2} (s-1) + \log \frac{w_1}{w_2} \right)^2 \right] \\ g(m, \sigma) &= \mathbb{E}_{x \sim \mathcal{N}(0,1)} \left[1 - 2 \text{expit} \left(2\sigma Rx + 2R^2m + \log \frac{w_*}{1-w_*} \right) \right] \end{aligned} \quad (\text{C.19})$$

we can conveniently write the gradient flow as:

$$\nabla_{\mu_1}^{\mathbb{S}} \mathcal{D}_{KL} = \frac{\mu_2 - \mu_1 s}{\sigma^2} f(s, \sigma) + \beta w_1 (\mu_* - m_1 \mu_1) g(m_1, \sigma). \quad (\text{C.20})$$

Using the symmetry $\mu_1 \rightarrow \mu_2$, $w_1 \rightarrow w_2$, we obtain the gradient with respect to μ_2 .

$$\nabla_{\mu_2}^{\mathbb{S}} \mathcal{D}_{KL} = \frac{\mu_1 - \mu_2 s}{\sigma^2} f(s, \sigma) + \beta w_2 (\mu_* - m_2 \mu_2) g(m_2, \sigma). \quad (\text{C.21})$$

Finally, we obtain the learning dynamics of the summary statistics by writing:

$$\begin{aligned} \dot{m}_1 &= \frac{\mu_* \cdot \mu_1}{R^2} = -\frac{\mu_*}{R^2} \cdot \nabla_{\mu_1}^{\mathbb{S}} \mathcal{D}_{KL} \\ &= - \left[\frac{(m_2 - m_1 s)}{\sigma^2} f(s, \sigma) + \beta w_1 (1 - m_1^2) g(m_1, \sigma) \right] \end{aligned} \quad (\text{C.22})$$

$$\begin{aligned} \dot{s} &= -\frac{1}{R^2} [\mu_2 \cdot \nabla_{\mu_1}^{\mathbb{S}} \mathcal{D}_{KL} + \mu_1 \cdot \nabla_{\mu_2}^{\mathbb{S}} \mathcal{D}_{KL}] \\ &= - \left[\frac{2(1-s^2)}{\sigma^2} f(s, \sigma) + \beta w_1 (m_2 - m_1 s) g(m_1, \sigma) + \beta w_2 (m_1 - m_2 s) g(m_2, \sigma) \right] \end{aligned} \quad (\text{C.23})$$

Using a quasi static approximation for the dynamics of the variances $\sigma = \beta(t)^{-\frac{1}{2}}$ we get:

$$\begin{aligned} \dot{m}_1 &= -\beta(t) \left[(m_2 - m_1 s) f(s, \beta(t)^{-\frac{1}{2}}) + w_1 (1 - m_1^2) g(m_1, \beta(t)^{-\frac{1}{2}}) \right] \\ \dot{m}_2 &= -\beta(t) \left[(m_1 - m_2 s) f(s, \beta(t)^{-\frac{1}{2}}) + w_2 (1 - m_2^2) g(m_2, \beta(t)^{-\frac{1}{2}}) \right] \\ \dot{s} &= -\beta(t) \left[2(1-s^2) f(s, \beta(t)^{-\frac{1}{2}}) + w_1 (m_2 - m_1 s) g(m_1, \beta(t)^{-\frac{1}{2}}) + w_2 (m_1 - m_2 s) g(m_2, \beta(t)^{-\frac{1}{2}}) \right] \end{aligned} \quad (\text{C.24})$$

Numerical integration of these coupled ODEs are in excellent agreement with trajectories obtained by SGD on both means and variances (fig. 3), confirming the validity of the variance approximation.

C.3 Low- and High-variance limits

Recall that since we approximated the variance:

$$\sigma_{1,2} = \beta^{-1} \quad (\text{C.25})$$

high and low variance limits correspond respectively to high and low temperature limits.

C.3.1 Low variance limit ($\sigma \ll R$)

Let's begin with f . We denote $r = \frac{R}{\sigma}$, $A = \sqrt{2(1-s)}$, $B = s-1 = -(1-s) = -\frac{A^2}{2}$, and $C = \log\left(\frac{w_2}{w_1}\right)$. We consider:

$$\begin{aligned}
& \mathbb{E}_{x \sim \mathcal{N}(0, I_d)} \left[\text{expit} \left(rAx - r^2 A^2/2 + C \right)^2 \right] \\
&= \mathbb{E}_{x \sim \mathcal{N}(-r^2 A^2/2 + C, rA)} \left[\text{expit}(x)^2 \right] \\
&= \int_{\mathbb{R}} \frac{dx}{\sqrt{2\pi}rA} e^{-\frac{(x+r^2 A^2/2-C)^2}{2r^2 A^2}} \text{expit}(x)^2 \\
&= \frac{1}{\sqrt{2\pi}rA} e^{-\frac{(r^2 A^2/2-C)^2}{2r^2 A^2}} \int_{\mathbb{R}} dx e^{-\frac{x^2}{2r^2 A^2}} e^{-x(1/2-C/r^2 A^2)} \text{expit}(x)^2 \\
&\sim \frac{1}{\sqrt{2\pi}rA} e^{-r^2 A^2/8} e^{C/2} \int_{\mathbb{R}} dx \frac{e^{-x/2}}{(1+e^{-x})^2} \sim \frac{\sqrt{\pi}}{4} \sqrt{\frac{w_2}{w_1}} \frac{1}{r\sqrt{1-s}} e^{-\frac{r^2(1-s)}{4}}
\end{aligned} \tag{C.26}$$

Recombining the different terms, this implies $f(s, \sigma) \sim \frac{\sqrt{\pi}}{2} \frac{\sqrt{w_1 w_2}}{r\sqrt{1-s}} e^{-\frac{r^2(1-s)}{4}}$

Let's now tackle g . Recall $\epsilon = \frac{1}{2R^2} \log \frac{w_*}{1-w_*}$.

$$\begin{aligned}
g(m, \sigma) &= \mathbb{E}_{x \sim \mathcal{N}(0, 1)} \left[1 - 2\text{expit} \left(2\sigma Rx + 2R^2 m + \log \frac{w_*}{1-w_*} \right) \right] \\
&= 1 - 2\mathbb{E}_{x \sim \mathcal{N}(0, 1)} \left[\text{expit} \left(2R^2 \left(\frac{\sigma}{R} x + m + \epsilon \right) \right) \right] \\
&= 1 - 2\mathbb{E}_{x \sim \mathcal{N}(0, 1/r)} \left[\text{expit} \left(2R^2(x + m + \epsilon) \right) \right] \\
&= 1 - 2\text{expit}(2R^2(m + \epsilon)) + \mathcal{O}(r^{-2})
\end{aligned} \tag{C.27}$$

(C.28)

Comparing the order of magnitude of f and g , the low variance dynamics are dominated by g which comes from the cross-entropy which attracts the means at $\pm\mu_*$.

C.3.2 High variance limit ($\sigma \gg R$)

We derive the high variance asymptotics of the entropic force f and the cross-entropic force g . We denote $r = R/\sigma$ and consider $r \rightarrow 0$. Let's begin with f and decompose it in the following way:

$$\begin{aligned}
f(s, \sigma) &= \mathbb{E}_{x \sim \mathcal{N}(0, I_d)} \left[w_1 \text{expit} \left(r\sqrt{2(1-s)}x + \log \frac{w_2}{w_1} \right)^2 + w_2 \text{expit} \left(r\sqrt{2(1-s)}x + \log \frac{w_1}{w_2} \right)^2 \right] \\
&+ \mathbb{E}_{x \sim \mathcal{N}(0, I_d)} \left[w_1 \text{expit} \left(r\sqrt{2(1-s)}x + r^2(s-1) + \log \frac{w_2}{w_1} \right)^2 + w_2 \text{expit} \left(r\sqrt{2(1-s)}x + r^2(s-1) + \log \frac{w_1}{w_2} \right)^2 \right] \\
&- \mathbb{E}_{x \sim \mathcal{N}(0, I_d)} \left[w_1 \text{expit} \left(r\sqrt{2(1-s)}x + \log \frac{w_2}{w_1} \right)^2 + w_2 \text{expit} \left(r\sqrt{2(1-s)}x + \log \frac{w_1}{w_2} \right)^2 \right]
\end{aligned} \tag{C.29}$$

For the first line, we make the change of variable $z = rx$. As $r \rightarrow 0$, we can use the asymptotic development of the convolution of a function with a gaussian of vanishing variance. As a result, the first line is equal to $w_1 \text{expit}(\frac{w_2}{w_1})^2 + w_2 \text{expit}(\frac{w_1}{w_2})^2 + \mathcal{O}(r^2) = w_1 w_2 + \mathcal{O}(r^2)$.

The difference between the second line and the third is bounded by Taylor equality at order 1. Using $\left| \text{expit} \left(r\sqrt{2(1-s)}x + r^2(s-1) + \log \frac{w_2}{w_1} \right)^2 - \text{expit} \left(r\sqrt{2(1-s)}x + \log \frac{w_2}{w_1} \right)^2 \right| < \|\text{expit}^2\|_\infty r^2(s-1) < r^2$, we obtain that the difference is $\mathcal{O}(r^2)$.

As a results, $f(s, \sigma) = w_1 w_2 + \mathcal{O}\left(\frac{R^2}{\sigma^2}\right)$ as $\frac{R}{\sigma} \rightarrow 0$, uniformly in s .

Let's continue with g . Recall that $\epsilon = \frac{1}{2R^2} \log \frac{w_*}{1-w_*}$. We decompose it in the following way:

$$\begin{aligned}
g(m, \sigma) &= \mathbb{E}_{x \sim \mathcal{N}(0,1)} \left[1 - 2\mathbb{1}_{\{2\sigma Rx + 2R^2m + \log \frac{w_*}{1-w_*} > 0\}} \right] \\
&\quad + \mathbb{E}_{x \sim \mathcal{N}(0,1)} \left[1 - 2\text{expit} \left(2\sigma Rx + 2R^2m + \log \frac{w_*}{1-w_*} \right) \right] - \mathbb{E}_{x \sim \mathcal{N}(0,1)} \left[1 - 2\mathbb{1}_{\{2\sigma Rx + 2R^2m + \log \frac{w_*}{1-w_*} > 0\}} \right] \\
&= \mathbb{E}_{x \sim \mathcal{N}(0,1)} \left[1 - 2\mathbb{1}_{\{x+r(m+\epsilon) > 0\}} \right] \\
&\quad + \mathbb{E}_{x \sim \mathcal{N}(0,1)} \left[1 - 2\text{expit} \left(2\sigma Rx + 2R^2m + \log \frac{w_*}{1-w_*} \right) \right] - \mathbb{E}_{x \sim \mathcal{N}(0,1)} \left[1 - 2\mathbb{1}_{\{x+r(m+\epsilon) > 0\}} \right]
\end{aligned} \tag{C.30}$$

The first term is straightforward and equal to $-\sqrt{\frac{2}{\pi}}r(m+\epsilon) + \mathcal{O}(r)$, by Taylor expanding the Gaussian density in 0. The second and the third term can be rewritten as:

$$\begin{aligned}
&\mathbb{E}_{x \sim \mathcal{N}(0,1)} \left[1 - 2\text{expit} \left(2\sigma Rx + 2R^2m + \log \frac{w_*}{1-w_*} \right) \right] - \mathbb{E}_{x \sim \mathcal{N}(0,1)} \left[1 - 2\mathbb{1}_{\{x+r(m+\epsilon) > 0\}} \right] \\
&= 2\mathbb{E}_{x \sim \mathcal{N}(0,1)} \left[-\text{expit} \left(2\sigma Rx + 2R^2m + \log \frac{w_*}{1-w_*} \right) + \mathbb{1}_{\{x+r(m+\epsilon) > 0\}} \right] \\
&= 2\mathbb{E}_{x \sim \mathcal{N}(2R^2(m+\epsilon), 2\sigma R)} \left[-\text{expit}(x) + \mathbb{1}_{\{x > 0\}} \right]
\end{aligned} \tag{C.31}$$

Note that the function $x \rightarrow -\text{expit}(x) + \mathbb{1}_{\{x > 0\}}$ is odd and decays exponentially as $|x| \rightarrow \infty$. Thus, we can Taylor expand the Gaussian density as a function of $\frac{1}{2\sigma R}$ near 0. Because even terms of this expansion are 0, we get that the first non vanishing term is of order $\mathcal{O}(\frac{r}{\sigma^2})$.

Comparing the order of magnitude of f and g , the high variance dynamics are dominated by f which comes from the entropy and drive μ_1 and μ_2 away.

D Mode collapse probability estimate

D.1 Linearization around $(m_1 = m_2 = 0, s = -1)$

We study here the high temperature ($\beta \ll R^{-2}$) dynamical regime of the dynamics. At initialization, in high dimensions, $m_1 \sim \mathcal{N}(0, 1/d)$ and $m_2 \sim \mathcal{N}(0, 1/d)$ are independent.

From the above high variance limits of f and g ,

$$f(s, \beta(t)^{-\frac{1}{2}}) = w_1 w_2 + \mathcal{O}(\beta R^2) \tag{D.1}$$

$$g(m, \beta(t)^{-\frac{1}{2}}) = -\sqrt{\frac{2}{\pi}} \beta^{\frac{1}{2}} R(m+\epsilon) + \mathcal{O}(\beta R^2). \tag{D.2}$$

We deduce that the high temperature dynamics are dominated by the entropic force f , driving the means apart and effectively projecting them onto the symmetric subspace $s = -1$ on a typical time scale $\mathcal{O}(w_1 w_2) = \mathcal{O}(1)$. As m_1 and m_2 typical initial values scale as $1/\sqrt{d}$ (considering $\sqrt{d} \gg 1$), once $s \approx -1$, the dynamics can be understood by linearizing the coupled ODEs of eq. (3.4) around the point $(m_1 = 0, m_2 = 0, s = -1)$. The time evolution of the sum and difference of m_1 and m_2 decouple from s :

$$\begin{aligned}
\dot{m}_1 + \dot{m}_2 &= - \left[2f(-1, \beta(t)^{-\frac{1}{2}}) + \frac{1}{2}g'(0, \beta(t)^{-\frac{1}{2}}) \right] (m_1 + m_2) - g(0, \beta(t)^{-\frac{1}{2}}) \\
\dot{m}_1 - \dot{m}_2 &= - \frac{1}{2}g'(0, \beta(t)^{-\frac{1}{2}})(m_1 - m_2) \\
\dot{s} &= - \left[4\delta s f(-1, \beta(t)^{-\frac{1}{2}}) + (m_1 + m_2)g(0, \beta(t)^{-\frac{1}{2}}) \right].
\end{aligned} \tag{D.3}$$

where $\delta s = s + 1$. We can explicitly solve the above linearized dynamical system for an arbitrary time dependant $\beta(t)$.

$$m_1(t) + m_2(t) = (m_1(0) + m_2(0)) e^{-\int_0^t ds a(s)} - \int_0^t ds b(s) e^{-\int_s^t du a(u)} \quad (\text{D.4})$$

$$m_1(t) - m_2(t) = (m_1(0) - m_2(0)) e^{-\int_0^t ds \frac{1}{2} g'(0, \beta(s)^{-\frac{1}{2}})} \quad (\text{D.5})$$

where $a(s) = 2f(-1, \beta(t)^{-\frac{1}{2}}) + \frac{1}{2}g'(0, \beta(t)^{-\frac{1}{2}})$ and $b(s) = g(0, \beta(t)^{-\frac{1}{2}})$.

Assuming the high temperature limit, $a(s) = w_1 w_2 + \mathcal{O}(\beta^{\frac{1}{2}} R)$ and $b(s) = \mathcal{O}(\beta^{\frac{1}{2}} R)$. Hence, the sum $m_1(t) + m_2(t)$ is of order $\mathcal{O}(\beta^{\frac{1}{2}} R)$.

On the other hand, the difference $m_1 - m_2$ is unstable since $-g'(0, \beta(t)^{-\frac{1}{2}}) = \sqrt{\frac{2}{\pi}} \beta^{\frac{1}{2}} R + \mathcal{O}(\beta R^2) > 0$. We have

$$m_1(t) - m_2(t) = (m_1(0) - m_2(0)) e^{\int_0^t ds \sqrt{\frac{\beta(s) R^2}{2\pi}}} + \mathcal{O}(\beta R^2). \quad (\text{D.6})$$

D.2 Mode collapse probability

We derive the theoretical estimate of the mode collapse probability, assuming that the transition from the high-temperature regime to the low temperature is really abrupt and occurs at $\beta = \alpha R^{-2}$.

Given an annealing schedule $\beta(t)$, we denote t_1 such that $\beta(t_1) = \alpha R^{-2}$. In other words, we suppose that for $t < t_1$, the dynamics can be described by the high temperature limit $\beta \ll R^{-2}$, and that for $t > t_1$, the dynamics can be described by the low temperature limit.

Leveraging the high temperature linearization of the dynamics until $t = t_1$, with a good approximation we have:

$$m_1(t_1) + m_2(t_1) \ll 1 \quad (\text{D.7})$$

$$m_1(t_1) - m_2(t_1) = (m_1(0) - m_2(0)) e^{\int_0^{t_1} ds \sqrt{\frac{\beta(s) R^2}{2\pi}}}. \quad (\text{D.8})$$

For $t > t_1$, the dynamics is described by the low temperature limit, which means that the asymptotic fate of m_1 and m_2 are governed by the sign of $m_1(t_1) + \epsilon$ and $m_2(t_1) + \epsilon$ respectively. Mode collapse is avoided if $\min(m_1(t_1), m_2(t_1)) < -\epsilon$ and $\max(m_1(t_1), m_2(t_1)) > -\epsilon$. The previous condition is achieved if (recall eq. (D.8)):

$$|m_1(t_1) - m_2(t_1)| > 2\epsilon \iff |m_1(0) - m_2(0)| > 2\epsilon e^{-\int_0^{t_1} ds \sqrt{\frac{\beta(s) R^2}{2\pi}}}. \quad (\text{D.9})$$

Since $m_1(0) - m_2(0)$ is the sum of two Gaussians of variance $1/d$ (in high dimensions), it is a Gaussian of variance $2/d$. Hence, we can compute the mode collapse probability $p(\beta)$:

$$p(\beta) = \int_{-2\epsilon e^{-I(t_1)}}^{2\epsilon e^{-I(t_1)}} dx \sqrt{\frac{d}{4\pi}} e^{-\frac{dx^2}{4}} \quad (\text{D.10})$$

where we define:

$$I(\beta) = \int_0^{t_1} ds \sqrt{\frac{\beta(s) R^2}{2\pi}}.$$

D.3 Focus on the exponential annealing schedule

Let's focus on the particular case of an exponential annealing schedule of the form:

$$\beta(t) = \min(\beta_i^{1-t/t_0}, 1). \quad (\text{D.11})$$

Then,

$$\int_0^{t_1} ds \sqrt{\beta(s)} = \sqrt{\beta_i} \int_0^{t_1} ds e^{-\frac{t}{t_0} \log \beta_i} = \frac{2t_0}{\log 1/\beta_i} \left[\frac{\sqrt{\alpha}}{R} - \sqrt{\beta_i} \right]. \quad (\text{D.12})$$

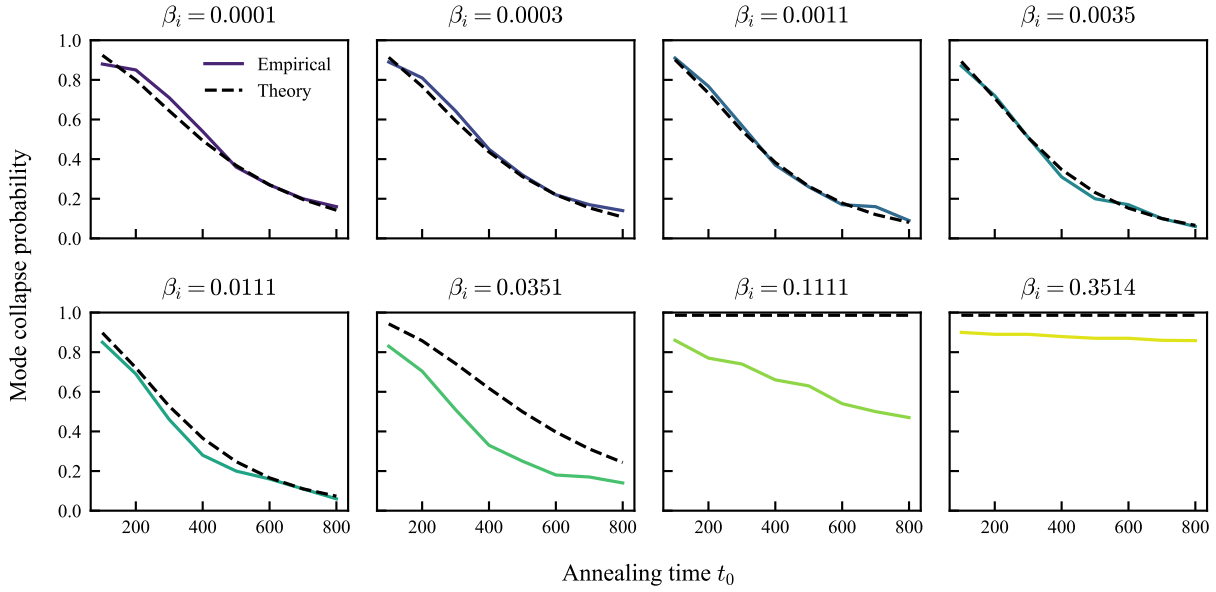


Figure 7: *Collapse probability for different initial temperatures, for Gaussian mixture student with an exponential annealing schedule.* Coloured curves are experimental mode collapse probability computed over 100 random student mean initialization. The experimental data are the same as in fig. 2. The dashed black line is the theoretical mode collapse probability eq. (3.7), with $\alpha = 0.608$. Hyperparameters are $d = 512$, $R = 3$, and $w_* = 0.8$.

This yields

$$I(\beta_i, t_0) = \sqrt{\frac{2}{\pi}} \frac{t_0}{\log 1/\beta_i} \left[\sqrt{\alpha} - \sqrt{R^2 \beta_i} \right]. \quad (\text{D.13})$$

Reinjecting this integral into eq. (D.10) we obtain a family of theoretical estimates of the mode collapse probability parametrized by α . Since α/R^2 corresponds to the end of the high temperature dynamical regime, we expect it to be of order one. fig. 7 shows the agreement with the experimental curves when setting $\alpha \approx 0.608$. The agreement for high initial temperature (low β_i) is excellent. The agreement worsens as β_i is increased to $1/R^2$, as expected since the high temperature dynamical regime description becomes less and less valid.

The success of annealing depends on maximizing the integral $I(\beta_i, t_0)$. The dependence with respect to t_0 is linear and intuitive: the longer the annealing time, the better. The integral has a unique global optimum with respect to β_i .

$$\begin{aligned} \frac{\partial I(\beta_i, t_0)}{\partial \beta_i} = 0 \iff & \frac{1}{2} R - \frac{R\sqrt{\beta_i} - \sqrt{\alpha}}{\sqrt{\beta_i} \log \beta_i} = 0 \\ \log(\beta_i/e) \frac{\beta_i}{e} = & \frac{-\sqrt{\alpha}}{eR} \\ \beta_i = e^2 W_0^2 \left(-\frac{\sqrt{\alpha}}{eR} \right) \end{aligned} \quad (\text{D.14})$$

where W_0 is the Lambert W_0 function defined by $W_0(z)e^{W_0(z)} = z$. On the real axis $W_0(x) < x$, and $W_0(x) \sim x$ as $x \rightarrow 0$.

Hence the optimal value of the initial temperature β_i is such that $\beta_i < \alpha/R^2$ and $\beta_i \sim \alpha/R^2$ as $R \rightarrow \infty$.

We now focus on the limit where the initial temperature is high ($\beta_i \ll R^{-2}$) —which is not optimal but relevant to practical cases when the true R is a priori unknown. We have:

$$I(\beta_i, t_0) \sim \sqrt{\frac{2}{\pi}} \frac{t_0 \sqrt{\alpha}}{\log 1/\beta_i}. \quad (\text{D.15})$$

Asymptotically, the value of the integral only depends on the inverse of the logarithm of the annealing rate β_i^{-1/t_0} . This is expected since the higher the annealing rate, the faster the temperature will go to 1. Notably, it implies that if the initial temperature is high enough, the relevant quantity for the success of annealing is the annealing rate. fig. 5 reports the probability of mode collapse with respect to the annealing rate. Increasing temperature curves rapidly collapse towards the asymptotic regime where mode collapse probability depends only on the annealing rate.